

A Node-Based Element for Analysis of Planar Piezoelectric Structures

H. Nguyen-Van¹, N. Mai-Duy¹ and T. Tran-Cong¹

Abstract: A novel node-based smoothing element for triangular and quadrilateral meshes is presented for static analysis of planar piezoelectric structures. In contrast to the smoothed finite element formulation that was based on sub-cells within an original quadrilateral element, this new method transforms a general original finite element mesh into a mesh of new smoothing cells individually associated with a single node which is termed as node-based elements. The displacement fields of the element are approximated by the linear interpolation functions of the original mesh while the approximations of mechanical strains and electric potential fields are normalized using the stabilized conforming nodal integration technique over each node-based element. This technique allows field gradients to be directly computed from interpolating shape functions by using boundary integrations along each edge of the node-based element. Furthermore, the present elements do not require any additional degrees of freedom and are insensitive to bad element shapes in the original mesh. Several numerical examples and comparative studies with other numerical results as well as analytic solutions in the literature are carried out in order to demonstrate the simplicity, efficiency and reliability of the novel elements.

Keyword: piezoelectric structures, node-based smoothed finite element, adaptive material, electro-mechanics.

1 Introduction

Piezoelectric materials have many applications in various modern engineering fields such as smart structures, mechatronics, ultrasonic transducers or micro-electromechanical system (MEMS) technology. It is evident that they have attracted significant attention of researchers. Many models and methods have been proposed over past decades towards better understanding of electromechanical coupling behaviour of piezoelectric materials including analytic/numerical methods and experimental models. Since only a few simple problems can be solved analytically [Crawley and

¹ CESRC, Faculty of Engineering & Surveying, USQ, Australia.

Luis (1987); Im and Atluri (1989); Shen (1995); Tzou and Tiersten (1994); Bisegna and Maceri (1996); Ray, Bhattacharya, and Samanta (1998); Lam and Ng (1999), several finite element methods (FEM) for coupled electro-mechanical systems have appeared in the literature such as Allik and Hughes (1970), Sze and Pan (1999); Sze and Yao (2000); Wu, Sze, and Huang (2001); Sze, Yang, and Yao (2004) and Cannarozzi and Ubertini (2001). More details and reviews on the development of the FEM applied to the modeling and analysis of piezoelectric material and smart structures can be found in Mackerle (2003). Some new special elements are still being developed as can be seen from recent works of Benjeddou (2000), Carrera and Boscolo (2007).

Although the FEM is considered to be a versatile and effective numerical method, there often exist difficulties and deteriorations in performance when mesh distortion occurs. On the other hand, several mesh-free methods have become an alternative approach for analysis of piezoelectric material, including the Radial Point Interpolation Meshfree (RIPM) method of Liu, Dai, Lim, and Gu (2003), the Point Interpolation Meshfree (PIM) method of Liu, Dai, Lim, and Gu (2002), the Point Collocation Meshfree (PCM) method of Ohs and Aluru (2001), the Element Free Galerkin (EFG) method of Liew, Lim, Tan, and He (2002), the Meshless Local Petrov-Galerkin (MLPG) method of Sladek, Sladek, Zhang, Garcia-Sanche, and Wunsche (2006); Sladek, Sladek, Zhang, Solek, and Starek (2007), etc.

A recent meshless technique is the stabilized conforming nodal integration (SCNI) mesh-free method [Chen, Wu, and You (2001)]. The application of the SCNI in the FEM was first proposed by Liu et al. [Liu, Dai, and Nguyen (2007); Liu, Nguyen, Dai, and Lam (2007); Dai, Liu, and Nguyen (2007); Dai and Liu (2007)] for 2D elasticity and further for laminated composite plates [Nguyen-Van, Mai-Duy, and Tran-Cong (2007), Nguyen-Van, Mai-Duy, and Tran-Cong (2008b)] and piezoelectric problems by Nguyen-Van, Mai-Duy, and Tran-Cong (2008a). It is found that the FEM, integrated with the SCNI technique, achieves more accurate results as compared with the conventional one without increasing the modelling and computational costs.

In this study, an alternative approach to incorporate the SCNI technique into the FEM is developed to formulate an efficient node-based smoothing element for analysis of planar piezoelectric structures. The proposed elements are created from a finite element mesh of triangular or quadrilateral elements and each of these new elements is associated with a single node of the original mesh. These node-based elements are generated in a similar way to the generation of background cells used for nodal integration in the meshfree radial point interpolation method of Liu, Zhang, Wang, Zhong, Li, and Han (2007). When only triangular elements are used, the proposed element is similar to the node-based uniform strain element proposed by

Dohrmann, Heinstein, Jung, Key, and Witkowski (2000). However, the significant distinguishing character of the present node-based elements is that the strains are normalized using the SCNI technique over the boundary of each smoothing cell, while the node-based uniform strain element approach requires the strains to be computed within each element using nodal averaging technique.

In comparison with the cell-based piezoelectric quadrilateral element (SPQ4) using the same SCNI technique [Nguyen-Van, Mai-Duy, and Tran-Cong (2008a)], the present node-based piezoelectric elements differ in the way that the smoothed cell is built to perform smoothing operations. While the cell-based element (SPQ4) is based on the subdivision of original quadrilateral finite elements, the node-based element is created by transforming a given more general mesh (triangular or quadrilateral elements) into a mesh of new smoothing cells each associated with a single node. Problem domains, therefore, can be discretized in more flexible ways. The displacement fields of the node-based element are approximated by linear interpolation functions of the original mesh while the approximations of mechanical strains and electric potential fields are normalized using the SCNI technique over each node-based element surrounding a single node. With a constant smoothing function, domain integrations can be changed into boundary integrations and field gradients can be directly computed from interpolating shape functions. No mapping or coordinate transformation and derivatives of shape functions are necessary so that the original meshes can be used even with badly shaped elements. Furthermore, the present elements do not introduce any additional degrees of freedom and stresses can be computed directly at field nodes.

Several numerical examples and comparison with other numerical or analytic solutions in the literature are carried out to demonstrate the capability, efficiency and reliability of the present novel element. Numerical experiment does show that the proposed element is robust and uniformly accurate in modelling static behavior of planar electro-mechanical problems even in the case of extremely distorted meshes or coarse discretization.

The remainder of the paper is outlined as follows. First, a brief review of a two-dimensional piezoelectric finite element formulation is presented in Section 2. The description of the node-based smoothing method for piezoelectric material is derived in Section 3. Several numerical applications are carried out in Section 4 to assess the performances of the proposed element. Finally, some concluding remarks are made in Section 5.

2 Review of a finite element formulation for 2D piezoelectric problems

In this section, the principal equations of piezoelectricity and finite element formulation for two-dimensional piezoelectric problems are briefly reviewed. A two-dimensional piezoelectric problem in domain Ω bounded by Γ is considered.

The mechanical constitutive relation for 2D piezoelectric materials can be expressed in the e -form as

$$\boldsymbol{\sigma} = \mathbf{c}_E \boldsymbol{\varepsilon} - \mathbf{e}^T \mathbf{E}, \quad (\text{converse effect}) \quad (1)$$

$$\mathbf{D} = \mathbf{e} \boldsymbol{\varepsilon} + \mathbf{g} \mathbf{E}, \quad (\text{direct effect}) \quad (2)$$

where $\boldsymbol{\sigma}$, $\boldsymbol{\varepsilon}$, \mathbf{D} and \mathbf{E} are the plane stress tensor, the plane strain tensor, the plane electric displacement vector and the plane electric field vector, respectively. \mathbf{c}_E , \mathbf{e} and \mathbf{g} are the plane elastic stiffness, piezoelectric and dielectric tensor, respectively.

Equations (1)–(2) can be rewritten in the explicit form in the $x-z$ plane as

$$\begin{bmatrix} \sigma_x \\ \sigma_z \\ \tau_{xz} \end{bmatrix} = \begin{bmatrix} c_{11} & c_{13} & 0 \\ c_{13} & c_{33} & 0 \\ 0 & 0 & c_{55} \end{bmatrix} \begin{bmatrix} \varepsilon_x \\ \varepsilon_z \\ \gamma_{xz} \end{bmatrix} - \begin{bmatrix} 0 & e_{31} \\ 0 & e_{33} \\ e_{15} & 0 \end{bmatrix} \begin{bmatrix} E_x \\ E_z \end{bmatrix}, \quad (3)$$

$$\begin{bmatrix} D_x \\ D_z \end{bmatrix} = \begin{bmatrix} 0 & 0 & e_{15} \\ e_{31} & e_{33} & 0 \end{bmatrix} \begin{bmatrix} \varepsilon_x \\ \varepsilon_z \\ \gamma_{xz} \end{bmatrix} + \begin{bmatrix} g_{11} & 0 \\ 0 & g_{33} \end{bmatrix} \begin{bmatrix} E_x \\ E_z \end{bmatrix}. \quad (4)$$

The finite element approximation solution for 2D piezoelectric problems using the standard linear element can be expressed as

$$\mathbf{u} = \sum_{i=1}^{np} \mathbf{N}_u^i \mathbf{q}_i = \mathbf{N}_u \mathbf{q}, \quad (5)$$

$$\phi = \sum_{i=1}^{np} \mathbf{N}_\phi^i \phi_i = \mathbf{N}_\phi \boldsymbol{\phi}, \quad (6)$$

where np is the number of nodes of an element; \mathbf{q} , $\boldsymbol{\phi}$ are the nodal displacement and nodal electric potential vectors and \mathbf{N}_u , \mathbf{N}_ϕ are shape function matrices.

The corresponding approximation of the linear strain $\boldsymbol{\varepsilon}$ and electric field \mathbf{E} are

$$\boldsymbol{\varepsilon} = \nabla_s \mathbf{u} = \begin{bmatrix} \frac{\partial}{\partial x} & 0 \\ 0 & \frac{\partial}{\partial z} \\ \frac{\partial}{\partial z} & \frac{\partial}{\partial x} \end{bmatrix} \mathbf{u} = \mathbf{B}_u \mathbf{q}, \quad (7)$$

$$\mathbf{E} = -\nabla \phi = -\mathbf{B}_\phi \boldsymbol{\phi}, \quad (8)$$

where

$$\mathbf{B}_u^i = \begin{bmatrix} N_{i,x} & 0 \\ 0 & N_{i,z} \\ N_{i,z} & N_{i,x} \end{bmatrix}, \quad (9)$$

$$\mathbf{B}_\phi^i = \begin{bmatrix} N_{i,x} \\ N_{i,z} \end{bmatrix}. \quad (10)$$

By using Hamilton's principle, the piezoelectric dynamic equations of an element can be obtained as

$$\begin{bmatrix} \mathbf{M}_{uu}^e & 0 \\ 0 & 0 \end{bmatrix} \begin{Bmatrix} \ddot{\mathbf{q}} \\ \ddot{\phi} \end{Bmatrix} + \begin{bmatrix} \mathbf{K}_{uu}^e & \mathbf{K}_{u\phi}^e \\ \mathbf{K}_{u\phi}^e & \mathbf{K}_{\phi\phi}^e \end{bmatrix} \begin{Bmatrix} \mathbf{q} \\ \phi \end{Bmatrix} = \begin{Bmatrix} \mathbf{F} \\ \mathbf{Q} \end{Bmatrix}, \quad (11)$$

in which

$$\mathbf{M}_{uu}^e = \int_{\Omega} \rho \mathbf{N}_u^T \mathbf{N}_u d\Omega, \quad (12)$$

$$\mathbf{K}_{uu}^e = \int_{\Omega} \mathbf{B}_u^T \mathbf{c}_E \mathbf{B}_u d\Omega, \quad (13)$$

$$\mathbf{K}_{u\phi}^e = \int_{\Omega} \mathbf{B}_u^T \mathbf{e}^T \mathbf{B}_\phi d\Omega, \quad (14)$$

$$\mathbf{K}_{\phi\phi}^e = - \int_{\Omega} \mathbf{B}_\phi^T \mathbf{g} \mathbf{B}_\phi d\Omega, \quad (15)$$

$$\mathbf{F} = \int_{\Omega} \mathbf{N}_u^T \mathbf{f} d\Omega + \int_{\Gamma_\sigma} \mathbf{N}_u^T \bar{\mathbf{t}} d\Gamma, \quad (16)$$

$$\mathbf{Q} = \int_{\Gamma_q} \mathbf{N}_\phi^T \bar{\mathbf{q}} d\Gamma. \quad (17)$$

where \mathbf{f} , $\bar{\mathbf{t}}$ are the vectors of mechanical body and surface forces, respectively; $\bar{\mathbf{q}}$ is the vector of surface charges.

For the static analysis ($\ddot{\mathbf{q}} = 0$), the governing equation of motion (11) is reduced to

$$\begin{bmatrix} \mathbf{K}_{uu}^e & \mathbf{K}_{u\phi}^e \\ \mathbf{K}_{u\phi}^e & \mathbf{K}_{\phi\phi}^e \end{bmatrix} \begin{Bmatrix} \mathbf{q} \\ \phi \end{Bmatrix} = \begin{Bmatrix} \mathbf{F} \\ \mathbf{Q} \end{Bmatrix}. \quad (18)$$

3 Node-based smoothing approach for piezoelectric finite element method

3.1 Smoothing technique

Consider a problem domain Ω with a mesh of triangular or quadrilateral elements numbered from 1 to N_e and nodes numbered from 1 to N_n . The basic idea of the following development is to associate new elements (smoothing elements) with each

of the nodes of the original mesh. For this process, the problem domain is transformed into smoothing cells associated with nodes such that $\Omega = \Omega^1 \cup \Omega^2 \cup \dots \cup \Omega^n$ and $\Omega^i \cap \Omega^j = \emptyset$, $i \neq j$. A new element (smoothing cell) Ω^k associated with a single node k is termed as the node-based element. These elements are created by connecting sequentially the mid-side points of edges emanating from node k to the centroidal points of original elements surrounding node k as shown in Figure 1.

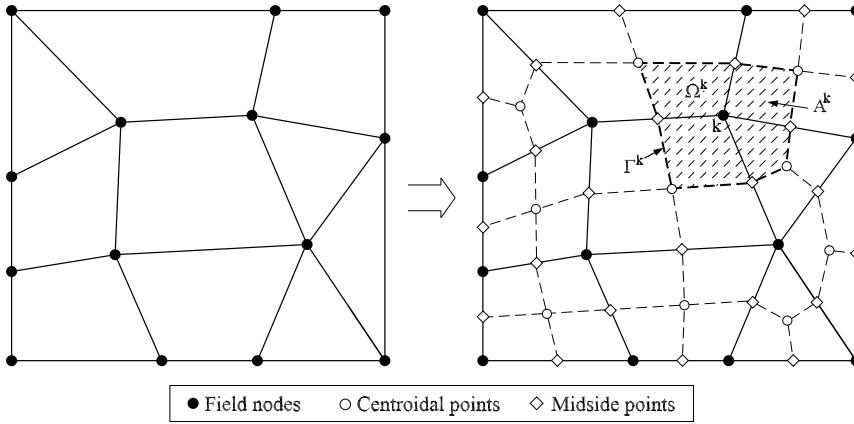


Figure 1: Node-based elements: Transformation of an original mesh into smoothing elements associated with nodes. The dashed lines are formed by connecting midside points with centroidal points of original elements and serve as new cell (element) boundaries.

Introducing the smoothing operation of the SCNI, the strain and electric fields over the smoothing cell Ω^k associated with node k are assumed as follows.

$$\tilde{\boldsymbol{\epsilon}}^k(\mathbf{x}^k) = \int_{\Omega^k} \boldsymbol{\epsilon}(\mathbf{x}) \Phi^k(\mathbf{x} - \mathbf{x}^k) d\Omega, \quad (19)$$

$$\tilde{\mathbf{E}}^k(\mathbf{x}^k) = \int_{\Omega^k} \mathbf{E}(\mathbf{x}) \Phi^k(\mathbf{x} - \mathbf{x}^k) d\Omega, \quad (20)$$

where $\boldsymbol{\epsilon}$, \mathbf{E} are respectively the mechanical strain and electric field obtained from displacement compatibility condition as given in Equations (7) and (8). Φ^k is a smoothing function that satisfies the following properties

$$\Phi^k \geq 0 \quad \text{and} \quad \int_{\Omega^k} \Phi^k d\Omega = 1. \quad (21)$$

For simplicity, Φ^k is chosen as a constant function

$$\Phi^k(\mathbf{x}-\mathbf{x}^k) = \begin{cases} 1/A^k & \mathbf{x} \in \Omega^k, \\ 0 & \mathbf{x} \notin \Omega^k. \end{cases} \quad (22)$$

where $A^k = \int_{\Omega^k} d\Omega$ is the area of the smoothing cell Ω^k as shown in Figure 1.

Substituting Φ^k into Equation (19)–(20) and applying the divergence theorem, we obtain a smoothed strain and smoothed electric field in the domain Ω^k as follows.

$$\tilde{\boldsymbol{\epsilon}}^k(\mathbf{x}^k) = \frac{1}{A^k} \int_{\Omega^k} \nabla_s \mathbf{u}(\mathbf{x}) d\Omega = \frac{1}{A^k} \int_{\Gamma^k} \mathbf{n}_u^k \mathbf{u}(\mathbf{x}) d\Gamma, \quad (23)$$

$$\tilde{\mathbf{E}}^k(\mathbf{x}^k) = -\frac{1}{A^k} \int_{\Omega^k} \nabla \phi(\mathbf{x}) d\Omega = -\frac{1}{A^k} \int_{\Gamma^k} \mathbf{n}_\phi^k \phi(\mathbf{x}) d\Gamma, \quad (24)$$

where \mathbf{n}_u^k and \mathbf{n}_ϕ^k are matrices associated with unit outward normal to the boundary Γ^k ,

$$\mathbf{n}_u^k = \begin{bmatrix} n_x^k & 0 \\ 0 & n_z^k \\ n_z^k & n_x^k \end{bmatrix}, \quad \mathbf{n}_\phi^k = \begin{bmatrix} n_x^k \\ n_z^k \end{bmatrix}, \quad (25)$$

and $\mathbf{u}(\mathbf{x})$, $\phi(\mathbf{x})$ are approximated functions as in Equations (5)–(6).

Introducing the finite element approximation of \mathbf{u} and ϕ into Equations (23) and (24), the smoothed strains on the smoothing cell Ω^k associated with the node k can be expressed in the following matrix form

$$\tilde{\boldsymbol{\epsilon}}^k(\mathbf{x}^k) = \sum_{i=1}^{nk} \tilde{\mathbf{B}}_u^i(\mathbf{x}^k) \mathbf{q}_i, \quad (26)$$

$$\tilde{\mathbf{E}}^k(\mathbf{x}^k) = -\sum_{i=1}^{nk} \tilde{\mathbf{B}}_\phi^i(\mathbf{x}^k) \phi_i, \quad (27)$$

in which nk is the number of nodes connecting directly to the node k (i.e. nodes whose shape functions support node k). $\tilde{\mathbf{B}}_{ui}(\mathbf{x}^k)$ and $\tilde{\mathbf{B}}_{\phi i}(\mathbf{x}^k)$ are smoothed gradient matrices for \mathbf{u} and ϕ respectively, on the smoothing cell Ω^k

$$\tilde{\mathbf{B}}_u^i(\mathbf{x}^k) = \frac{1}{A^k} \int_{\Gamma^k} \begin{bmatrix} N_i n_x^k & 0 \\ 0 & N_i n_z^k \\ N_i n_z^k & N_i n_x^k \end{bmatrix} d\Gamma, \quad (28)$$

$$\tilde{\mathbf{B}}_\phi^i(\mathbf{x}^k) = \frac{1}{A^k} \int_{\Gamma^k} \begin{bmatrix} N_i n_x^k \\ N_i n_z^k \end{bmatrix} d\Gamma. \quad (29)$$

When a linear completed displacement field along the boundary Γ^k is used, one Gauss point is sufficient for accurate boundary integration along each line segment Γ_i^k of the contour Γ^k of Ω^k . Therefore, Equations (28)–(29) can be evaluated with one-point Gauss quadrature integration as follows.

$$\tilde{\mathbf{B}}_u^i(\mathbf{x}^k) = \frac{1}{A^k} \sum_{b=1}^{nb} \begin{bmatrix} N_i(\mathbf{x}_b^G) n_x^k & 0 \\ 0 & N_i(\mathbf{x}_b^G) n_z^k \\ N_i(\mathbf{x}_b^G) n_z^k & N_i(\mathbf{x}_b^G) n_x^k \end{bmatrix} l_b^k, \quad (30)$$

$$\tilde{\mathbf{B}}_\phi^i(\mathbf{x}^k) = \frac{1}{A^k} \sum_{b=1}^{nb} \begin{bmatrix} N_i(\mathbf{x}_b^G) n_x^k \\ N_i(\mathbf{x}_b^G) n_z^k \end{bmatrix} l_b^k, \quad (31)$$

where nb is the total number of the line segments of the contour Γ^k , \mathbf{x}_b^G is the midpoint (Gauss point) of each line segments Γ_b^k , whose length and outward unit normal are denoted as l_b^k and \mathbf{n}^k , respectively.

Finally, the linear static equation (11) can be rewritten as follows

$$\begin{bmatrix} \tilde{\mathbf{K}}_{uu}^k & \tilde{\mathbf{K}}_{u\phi}^k \\ \tilde{\mathbf{K}}_{u\phi}^k & \tilde{\mathbf{K}}_{\phi\phi}^k \end{bmatrix} \begin{Bmatrix} \mathbf{u} \\ \phi \end{Bmatrix} = \begin{Bmatrix} \mathbf{F} \\ \mathbf{Q} \end{Bmatrix}, \quad (32)$$

where

$$\tilde{\mathbf{K}}_{uu}^k = \sum_{i=1}^{nk} \tilde{\mathbf{B}}_u^{iT} \mathbf{c}_E \tilde{\mathbf{B}}_u^i A^k, \quad (33)$$

$$\tilde{\mathbf{K}}_{u\phi}^k = \sum_{i=1}^{nk} \tilde{\mathbf{B}}_u^{iT} \mathbf{e}^T \tilde{\mathbf{B}}_\phi^i A^k, \quad (34)$$

$$\tilde{\mathbf{K}}_{\phi\phi}^k = - \sum_{i=1}^{nk} \tilde{\mathbf{B}}_\phi^{iT} \mathbf{g}^T \tilde{\mathbf{B}}_\phi^i A^k. \quad (35)$$

The stiffness matrix $\tilde{\mathbf{K}}$ of the system is then assembled in a manner similar to that in the conventional FEM such as

$$\tilde{\mathbf{K}} = \sum_{k=1}^{N_n} \tilde{\mathbf{K}}^k, \quad (36)$$

where

$$\tilde{\mathbf{K}}^k = \begin{bmatrix} \tilde{\mathbf{K}}_{uu}^k & \tilde{\mathbf{K}}_{u\phi}^k \\ \tilde{\mathbf{K}}_{u\phi}^k & \tilde{\mathbf{K}}_{\phi\phi}^k \end{bmatrix}. \quad (37)$$

It can be seen that only values of shape functions at Gauss points along the edges of boundary Γ_i^k are need for evaluating Equations (30)–(31). The details for computing values of shape functions are presented in the following section.

3.2 Linear shape functions

In this study, a finite element mesh of linear triangular or bilinear quadrilateral elements is considered. It should be noted that the purpose of introducing mid-side points and centroidal points is to form the linear compatible contour of the node-based element and to evaluate the shape functions at the Gauss points. No additional degrees of freedom are associated with these points and the nodal unknowns are the same as in the original FEM mesh. Moreover, the derivations of the smoothed strain and smoothed electric fields of the smoothing cell Ω^k associated with node k transforms the domain integration into line integration along the contour Γ^k of Ω^k . Therefore, only the shape function values at Gauss points along each edge Γ_i^k of the contour Γ^k are used. Values of shape functions at these points of interest (mid-edge points and centroidal points) for triangular and quadrilateral element are illustrated in Figure 2. Note that the shape function values in Figure 2 are denoted in the format $(N_1, N_2, \dots, N_{ne})$ where ne is the number of nodes of an element.

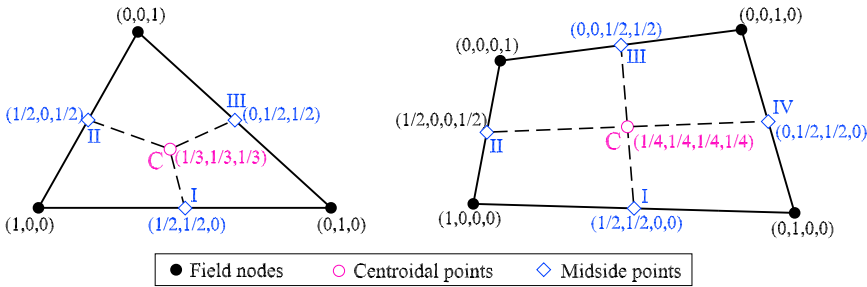


Figure 2: Shape function values for a typical linear triangular and bilinear quadrilateral element.

By using an original mesh of linear triangular or bilinear quadrilateral elements, a linear compatible displacement field along the boundary Γ^k of a smoothing cell (node-based element) is obtained. Only one Gauss point at midside point on each edge of Γ^k is required for accurate boundary integration. The shape function values at the Gauss points (e.g. point c) are shown in Figure 3.

3.3 Implementation procedure

In order to clarify how the node-based smoothing technique is incorporated into a finite element code, a numerical implementation for the method is briefly presented as follows.

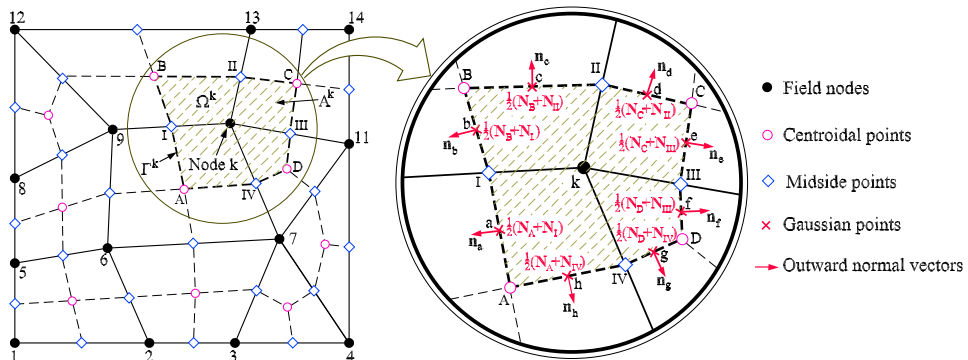


Figure 3: Detail of a node-based element (smoothing cell) and values of shape functions at Gauss points (a,b,c,d,e,f,g,h)

1. Discretize the domain into triangular or quadrilateral elements and get the matrices of nodes coordinates (**coord**) and element connections (**nodes**).
2. Find surrounding cells of each node k and determine the area of each smoothing cell Ω^k associated with node k :

Loop over all nodes, $k = 1$ to N_n

Loop over all elements, $j = 1$ to N_e

if (find ($k == \mathbf{nodes}(j, :)$)) ≥ 1 , add the element j to the list of surrounding cells and compute the area of the surrounding cell j .

End the loop over all elements.

End the loop over all nodes.

3. Calculate and assemble element stiffness matrices to build the system stiffness matrix:

Loop over all nodes, $k = 1$ to N_n

- (a) Determine the connecting points of each smoothing cell Ω^k associated with node k .
- (b) Calculate the outward unit normal vector \mathbf{n}^k on each boundary side of the smoothing cell Ω^k .
- (c) Evaluate smoothed gradient matrices $\tilde{\mathbf{B}}_u^k, \tilde{\mathbf{B}}_\phi^k$ using Equations (30)–(31).
- (d) Compute smoothed element stiffness matrices corresponding to the Ω^k using Equations (33)–(35).

- (e) Assemble the contribution of smoothed element stiffness matrices to form the system stiffness matrix using Equation (36).

End the loop over all nodes.

4. Assign boundary conditions.
5. Solve the system equation to obtain nodal kinematics.
6. Post-process strains and stresses at points of interest.

4 Numerical results

In this section, several numerical examples are employed to test and assess the performance of the node-based smoothing elements as applied to the linear static analysis of two-dimensional piezoelectric structures. The node-based smoothing piezoelectric element is termed as NSPE-T3 if based on triangular FE mesh and as NSPE-Q4 if based on quadrilateral FE mesh.

4.1 Patch testing

Passing the patch test is a sufficient condition for the convergence of a finite element method. It is an essential check in order to verify that the elements exhibit proper convergence properties, consistency and stability. In this section, a patch test is used to verify that the proposed node-based element, NSPE-T3 or NSPE-Q4, has proper convergence properties. A choice of geometry, mesh and boundary conditions was adopted from the work of Sze *et al.* Sze, Yang, and Yao (2004), as shown in Figure 4.

The following PZT4 material in Reference Sze, Yang, and Yao (2004) is used for the patch test.

$$c_{11} = 139 \times 10^3, \quad c_{33} = 113 \times 10^3, \quad c_{13} = 74.3 \times 10^3, \quad c_{55} = 25.6 \times 10^3 (N/mm^2),$$

$$e_{15} = 13.44 \times 10^6, \quad e_{31} = -6.98 \times 10^6, \quad e_{33} = 13.84 \times 10^6 (pC/mm^2),$$

$$g_{11} = 6.00 \times 10^9, \quad g_{33} = 5.47 \times 10^9 (pC/GVmm).$$

The prescribed mechanical displacements and electric potentials are applied at the edges defined by nodes 1, 2, 3 and 4 as follows.

$$u = s_{11}\sigma_0x, \quad w = s_{13}\sigma_0z, \quad \phi = b_{31}\sigma_0z.$$

where $\sigma_0 = 1000$ is an arbitrary stress parameter. s_{11} , s_{13} and b_{31} are material constants which can be calculated by the following relation

$$\begin{bmatrix} s_{11} & s_{13} & b_{31} \\ s_{13} & s_{33} & b_{33} \\ b_{31} & b_{33} & -f_{33} \end{bmatrix} = \begin{bmatrix} c_{11} & c_{13} & e_{31} \\ c_{13} & c_{33} & e_{33} \\ e_{31} & e_{33} & -g_{33} \end{bmatrix}^{-1}.$$

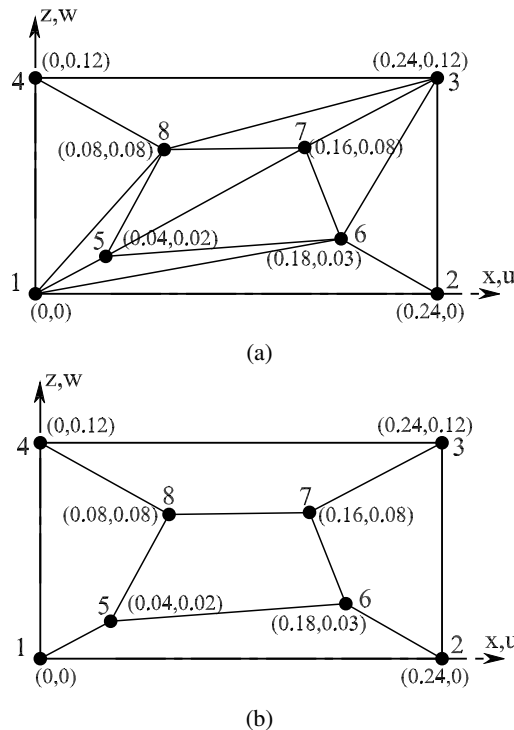


Figure 4: Typical meshes of the patch test: (a) triangular mesh (NSPE-T3 elements); (b) quadrilateral mesh (NSPE-Q4 elements).

Under the boundary conditions described above, the corresponding exact stress $\boldsymbol{\sigma}$ and electric displacement \mathbf{D} are given as: $\sigma_x = \sigma_0$, $\sigma_z = \tau_{xz} = D_x = D_z = 0$.

It is found that the obtained results with NSPE-T3 and NSPE-Q4 elements match well the exact solution as shown in Table 1 and hence the node-based elements successfully pass the patch test.

4.2 Single-layer piezoelectric strip in shear deformation

In this example, we consider the shear deformation of a $1 \times 1\text{mm}$ single-layer square strip polarized in the z -direction. The strip is subjected to a combined loading of pressure σ_0 in the z direction and an applied voltage V_0 as depicted on Figure 5. The material PZT-5 is used for this problem and its properties are summarized in Table 2.

The following mechanical and electrical boundary conditions were applied to the

Table 1: Results of the patch test.

	Results		
	NSPE-T3	NSPE-Q4	Exact
σ_x	1000.0000	1000.0000	1000
σ_z	2.0240×10^{-10}	-8.6968×10^{-14}	0
τ_{xz}	2.2414×10^{-10}	-4.1149×10^{-13}	0
D_x	-1.0658×10^{-8}	-2.2461×10^{-10}	0
D_z	5.5046×10^{-8}	1.1983×10^{-10}	0

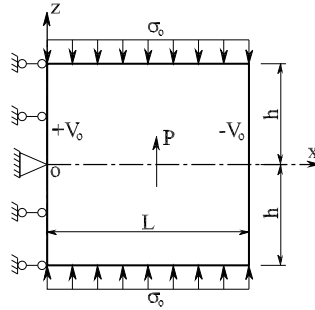


Figure 5: Piezo-strip subjected to a uniform stress and a voltage.

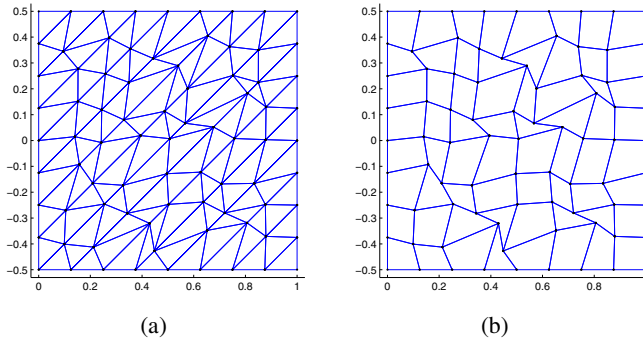


Figure 6: Typical meshes of a piezo-strip in shear: (a) triangular mesh (NSPE-T3 elements); (b) quadrilateral mesh (NSPE-Q4 elements).

sides of the strip

$$\begin{aligned}
 \phi_{,z}(x, \pm h) &= 0, & \sigma_z(x, \pm h) &= \sigma_0, & \tau_{xz}(L, z) &= 0, \\
 \tau_{xz}(x, \pm h) &= 0, & \phi(L, z) &= -V_0, & \sigma_x(L, z) &= 0, \\
 \phi(0, z) &= +V_0, & u(0, z) &= 0, & w(0, 0) &= 0.
 \end{aligned}$$

Table 2: Single-layer piezoelectric material properties, dimensions and other constants.

s_{11}	$16.4 \times 10^{-6} \frac{(mm)^2}{N}$	d_{31}	$-172 \times 10^{-9} \frac{mm}{V}$
s_{13}	$-7.22 \times 10^{-6} \frac{(mm)^2}{N}$	d_{33}	$-374 \times 10^{-9} \frac{mm}{V}$
s_{33}	$18.8 \times 10^{-6} \frac{(mm)^2}{N}$	d_{15}	$584 \times 10^{-9} \frac{mm}{V}$
s_{55}	$47.5 \times 10^{-6} \frac{(mm)^2}{N}$	g_{11}	$1.53105 \times 10^{-8} \frac{N}{V^2}$
σ_0	$-5.0 \frac{N}{mm^2}$	g_{33}	$1.505 \times 10^{-8} \frac{N}{V^2}$
σ_1	$20.0 \frac{N}{mm^2}$	V_0	1000V
L	1.0mm	h	0.5mm

The strip is modelled with two types of mesh in this analysis with 8×8 quadrilateral elements or triangular elements as shown in Figure 6.

The present numerical results are compared with the standard linear triangular piezoelectric finite element FEM-T3, the cell-based smoothed quadrilateral piezoelectric element SPQ4 [Nguyen-Van, Mai-Duy, and Tran-Cong (2008a)] and the exact solutions given by Gaudenzi and Bathe Gaudenzi and Bathe (1995). Figure 7a

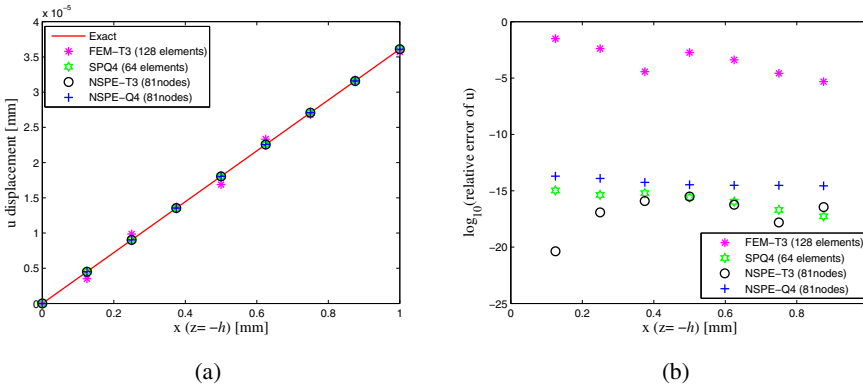


Figure 7: Piezo-strip in shear: Computed and exact u -displacements: (a) Distribution of u on the edge $z = -h$; (b) Comparison of the error of u -displacement.

and Figure 8a depict the distribution of the displacements u and w along the bottom edge ($z = -h$), respectively. The distribution of the computed electric potential ϕ along this edge is also demonstrated in Figure 9a. It is observed that all the computed displacements and electric potentials for both types of mesh are in excellent agreement with the analytical solutions.

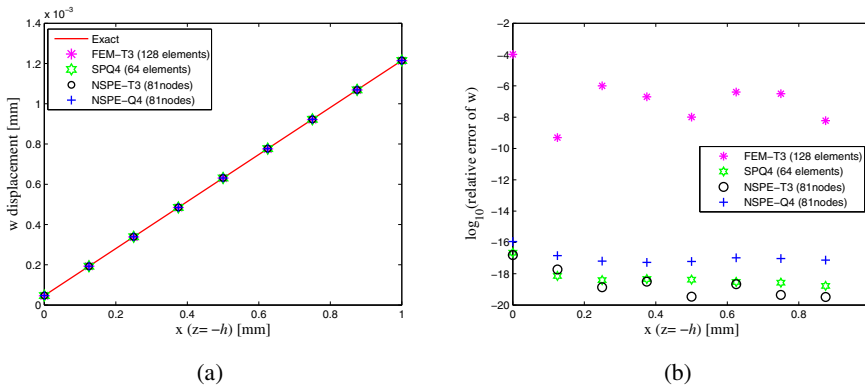


Figure 8: Piezo-strip in shear: Computed and exact w -displacements: (a) Distribution of w on the edge $z = -h$; (b) Comparison of the error of w -displacement.

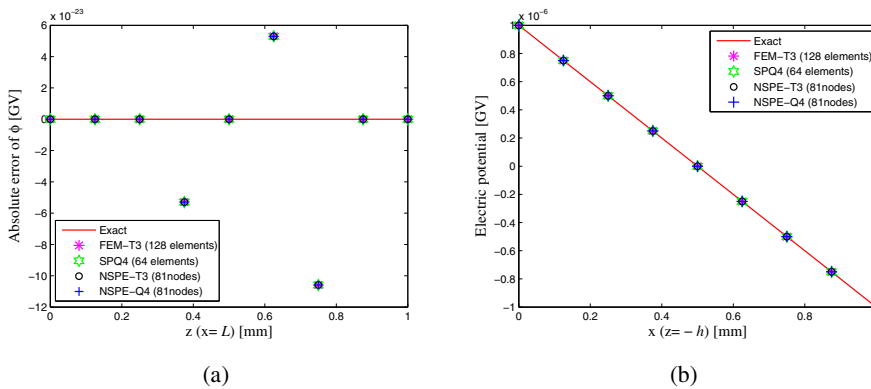


Figure 9: Piezo-strip in shear: Computed and exact electric potential ϕ : (a) Distribution of ϕ on the edge $z = -h$; (b) Comparison of the error of electric potential.

The relative errors (in log scale) of the displacements and electric potentials are illustrated on Figure 7b–Figure 9b. It can be seen that the node-based NSPE-T3 element achieves the best prediction for displacements (both of u and w) when compared with other numerical solutions. The superior accuracy of the present node-based elements (NSPE-T3 and NSPE-Q4 elements) over the standard FEM-T3 element is evident.

4.3 Single-layer piezoelectric strip in bending

The strip with the same material and geometry as in the previous example is considered but with modified boundary conditions for bending situation. In this case, a voltage V_0 is applied on the top and bottom surfaces together with a linear stress applied at the right edge as shown in Figure 10.

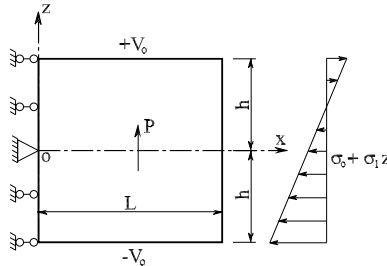


Figure 10: Piezo-strip subjected to a linear stress and a voltage.

The following mechanical and electrical boundary conditions are applied to the edges of the strip

$$\begin{aligned} \phi(x, \pm h) &= \pm V_0, \quad \sigma_z(x, \pm h) = 0, \quad \tau_{xz}(x, \pm h) = 0, \\ \phi_{,x}(L, z) &= 0, \quad \sigma_x(L, z) = \sigma_0 + \sigma_1 z, \quad \tau_{xz}(L, z) = 0, \\ \phi_{,x}(0, z) &= 0, \quad u(0, z) = 0, \quad w(0, 0) = 0. \end{aligned}$$

The analytical solution is available for this problem and can be found in Gaudenzi and Bathe (1995); Ohs and Aluru (2001). Two types of mesh as shown in Figure 6 are used again in the analysis.

Figure 11 illustrates the distribution of displacement u and its relative error along the right side ($x = L$) while the vertical displacement w and its relative error along the bottom edge ($z = -h$) are shown in Figure 12. The distribution of the computed electric potentials along the right side ($x = L$) and its relative error are demonstrated in Figure 13. Both computed displacements and electric potential match well the exact solutions for the node-based NSPE-T3 element as well as for the NSPE-Q4 element. Again, the node-based element NSPE-T3 demonstrates the best performance with respect to displacement fields when compared with the FEM-T3, SPQ4 and NSPE-Q4 elements as can be seen in the Figure 11b–Figure 12b. For the prediction of electric potential fields, all elements yield virtually identical results which appear indistinguishable from each other as can be seen in Figure 13.

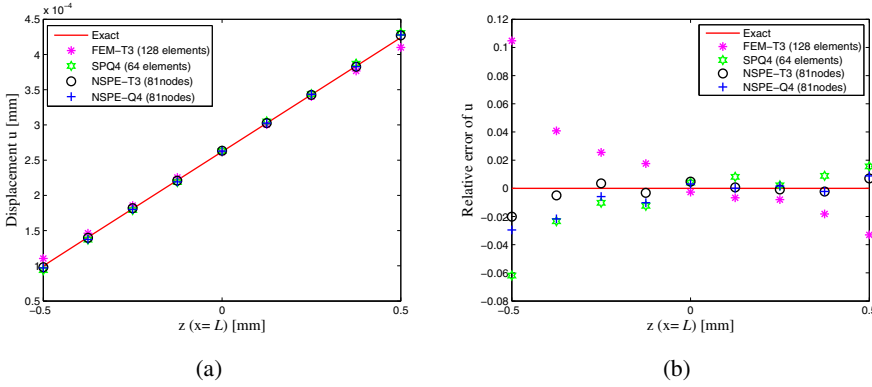


Figure 11: Piezo-strip in bending: Computed and exact u -displacements: (a) Distribution of u on the edge $x=L$; (b) Comparison of the error of u -displacement.

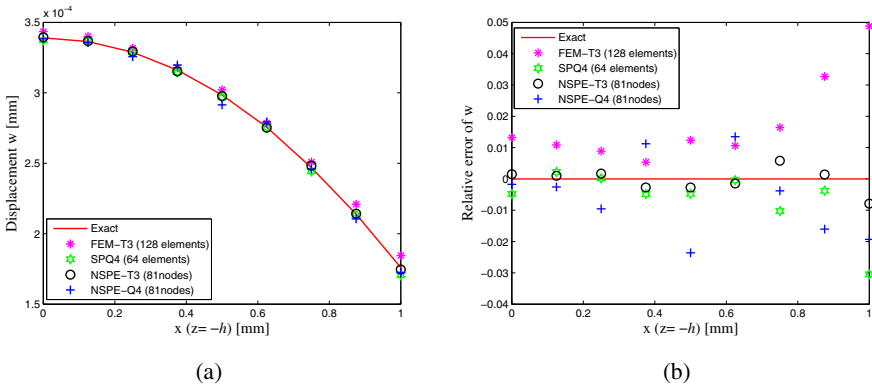


Figure 12: Piezo-strip in bending: Computed and exact w -displacements: (a) Distribution of w on the edge $z=-h$; (b) Comparison of the error of w -displacement.

4.4 A parallel piezoelectric bimorph beam

The example to be discussed here is the two-layer parallel bimorph beam. It consists of a cantilever piezoelectric beam made of two PVDF layers of the same thickness $h_t = h_b = H/2 = 0.2$ mm and a length of $L = 5$ mm, with same polarization orientations as shown in Figure 14. The PVDF material properties are summarized as follows.

$$\begin{aligned}
 E &= 2 \text{ GPa}, \nu = 0.29, e_{31} = 0.046 \text{ C/m}^2, \\
 e_{32} &= 0.046 \text{ C/m}^2, g_{11} = 0.1062 \times 10^{-9} \text{ F/m}, \\
 g_{33} &= 0.1062 \times 10^{-9} \text{ F/m}.
 \end{aligned}$$

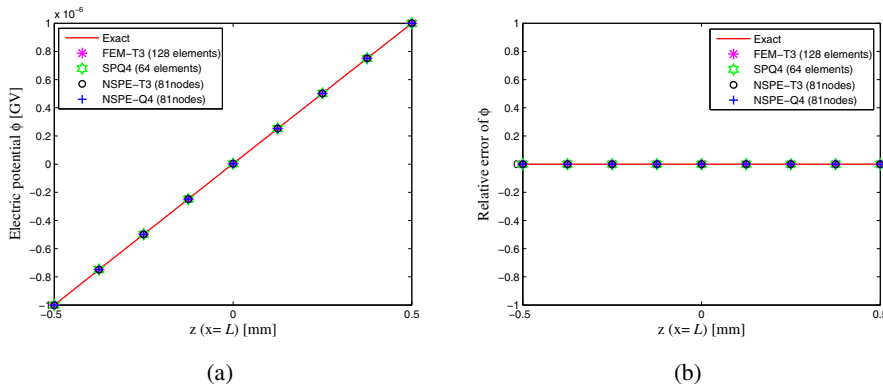


Figure 13: Piezo-strip in bending: Computed and exact electric potential ϕ : (a) Distribution of ϕ on the edge $x = L$; (b) Comparison of the error of electric potential.

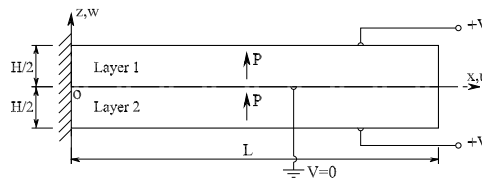


Figure 14: Two-layer parallel bimorph cantilever beam.

For the parallel bimorph configuration, a zero voltage ($V = 0$) is applied to the intermediate electrode, while the voltage $V = 1$ is applied to the bottom and top faces of the beam. As a result this will generate moments that bend the bimorph.

In this study, the beam is assumed to be in a plane stress state. For an applied electric field V only, the tip deflection δ of the cantilever parallel bimorph can be approximated as [Cambridge (1995)]

$$\delta = \frac{2L^2Vd_{31}}{H^2}. \tag{38}$$

With $L = 5$ mm and $H = 0.4$ mm, the approximated value of the tip deflection calculated from Equation (38) is $\delta = 1.0206 \times 10^{-8}$ (m).

The beam is analyzed using 15×2 , 25×2 , 35×2 and 50×2 uniform meshes of NSPE-T3 and NSPE-Q4 elements. Table 3 presents the obtained tip deflections together with meshless solutions such as PIM [Liu, Dai, Lim, and Gu (2002)] and RPIM [Liu, Dai, Lim, and Gu (2003)], the cell-based smoothed element SPQ4

Table 3: Tip deflections of the bimorph beam and comparison with available literatures ($\times 10^{-8}$ m).

Model	Mesh			
	15×2	25×2	35×2	50×2
FEM-T3	0.4967	0.6287	0.6785	0.7084 (-30.589%)
PIM	–	1.098	–	1.111 (8.856%)
RPIM	–	–	–	1.204 (17.970%)
SPQ4	0.814	0.937	0.978	1.003 (-1.724%)
NSPE-Q4	1.0321	1.0287	1.0275	1.0269 (0.617%)
NSPE-T3	1.0263	1.0276	1.0270	1.0264 (0.568%)
Analytic				1.0206

[Nguyen-Van, Mai-Duy, and Tran-Cong (2008a)] and the analytic solution. Note that the values in parentheses are the relative errors compared with analytic solutions. Numerical results in the Table 3 also indicate that the node-based element performance, in terms of rate of convergence and accuracy, with respect to exact solution is excellent.

Figure 15 depicts the relative error on tip deflection for different mesh refinement on a log scale. It is evident that the present NSPE-T3 element, gives more accurate results than those of other numerical solutions cited here where the displacement prediction error for the 50×2 mesh is only 0.568%. On the whole, all the node-based element perform similarly well and better than the cell-based SPQ4 element and the FEM-T3 element.

4.5 A piezoelectric Cook’s membrane

This section deals with a clamped tapered panel with distributed in-plane tip load $F = 1$ similar to the well-known Cook’s membrane. The lower surface is subjected to a voltage $V = 0$. The geometry and boundary conditions of the beam are shown in the Figure 16. The beam is made of PZT4 material as in Section 4.1.

The two typical types of mesh with 8×8 quadrilateral elements or triangular elements are shown in Figure 17.

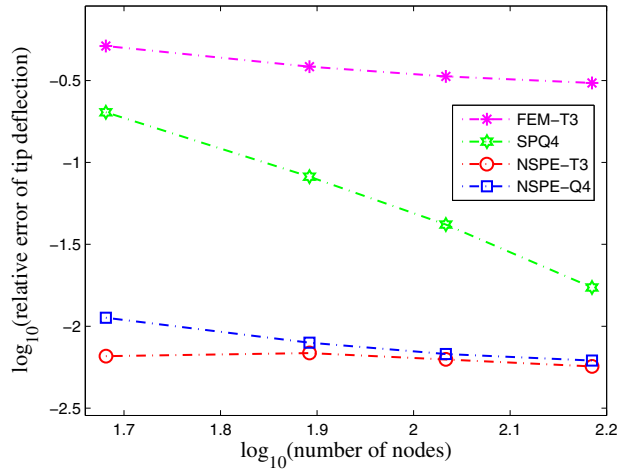


Figure 15: Convergence behaviour of tip deflection.

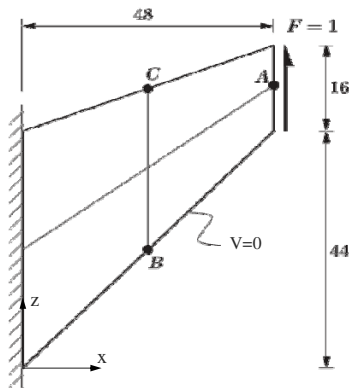


Figure 16: Piezoelectric Cook's membrane.

There is no analytic solution available for this problem. The present results are compared with the best known values of the displacement, the electric potential, the first principal stress and the electric flux density at node A, B, C according to Long, Loveday, and Groenwold (2006). They are summarized as follows.

$$w_A = 2.109 \times 10^{-4} \text{mm}, \phi_A = 1.732 \times 10^{-8} \text{GV},$$

$$\sigma_{1B} = 0.21613 \text{N/mm}^2, D_C = 22.409 \text{pC/mm}^2.$$

Table 4 presents the obtained results with mesh refinement and relative error (values in parentheses) when compared with the best known values of Long, Loveday, and

Table 4: Computed results of piezoelectric membrane and relative error percentage.

	Mesh	$w_A \times 10^{-4} (mm)$	$\phi_A \times 10^{-8} (GV)$	$\sigma_{1B} (N/mm^2)$	$D_C (pC/mm^2)$
NSPE-Q4	4 × 4	2.2414	2.2294	2.1982E-01	1.8898E+01
	8 × 8	2.1568	1.9565	2.1423E-01	2.1548E+01
	16 × 16	2.1204	1.8109	2.1476E-01	2.2133E+01
	24 × 24	2.1137 (0.223%)	1.7680 (2.078%)	2.1512E-01 (-0.453%)	2.2179E+01 (-1.026%)
NSPE-T3	4 × 4	2.2630	2.4646	3.8899E-01	3.2448E+01
	8 × 8	2.1688	1.9597	2.2729E-01	2.4441E+01
	16 × 16	2.1227	1.8177	2.1904E-01	2.1828E+01
	24 × 24	2.1156 (0.313%)	1.7622 (1.744%)	2.1696E-01 (0.398%)	2.1944E+01 (-2.075%)
FEM-T3	24 × 24	2.0046 (-4.950%)	1.6213 (-6.391%)	2.0955E-01 (-3.031%)	1.8476E+01 (-17.551%)
	SPQ4	24 × 24	2.1005 (-0.403%)	1.7033 (-1.657%)	2.1093E-01 (-2.392%)
Long <i>et al.</i> (2006)		2.109	1.732	0.2161	22.409

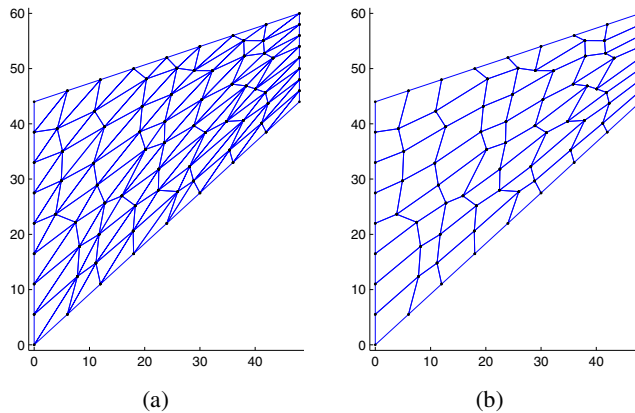


Figure 17: Typical meshes of a piezoelectric Cook's membrane: (a) triangular mesh (NSPE-T3 elements); (b) quadrilateral mesh (NSPE-Q4 elements).

Groenwold (2006). It can be seen that with a mesh of 24×24 , all the results of node-based elements achieve better accuracy (relative error within 2%) than those of the FEM-T3 element.

Figure 18a displays the magnitude of the relative error of vertical displacement w_A at point A with various meshes. The accuracy of the node-based element is again found to be better than the SPQ4 and FEM-T3 elements.

Figure 18b depicts the magnitude of the relative error of electric potential ϕ_A at point A. Again, the node-based elements is superior to the FEM-T3 elements. It is found that the cell-based SPQ4 element performs slightly better than the node-based elements in this case.

Figure 19 presents the magnitude of relative errors of the first principle stress σ_{1B} at point B and the electric flux density D_C at point C. Again, all the node-based elements perform similarly well and achieve better results than those of SPQ4 and FEM-T3 elements.

4.6 A double bimorph optical micro-scanner

An optical micro-scanner is usually composed of an adjustable mirror that is used to reflect light beams. It has a large variety of applications such as optical scanning, display devices, printer or barcode scanning. This section concerns the modelling of a simple micro-scanner, as depicted in Figure 20. The device is composed of two parallel bimorphs connected by a mirror at their tip center. When a voltage is

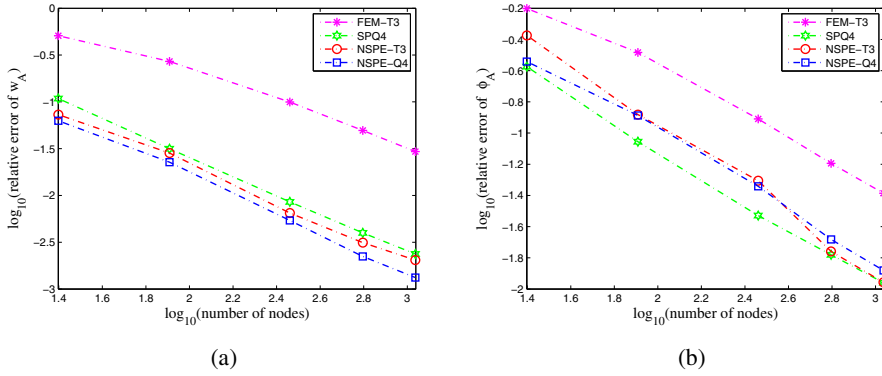


Figure 18: Piezoelectric Cook’s membrane: Convergence behaviours: (a) vertical displacement w at point A; (b) electric potential ϕ at point A.

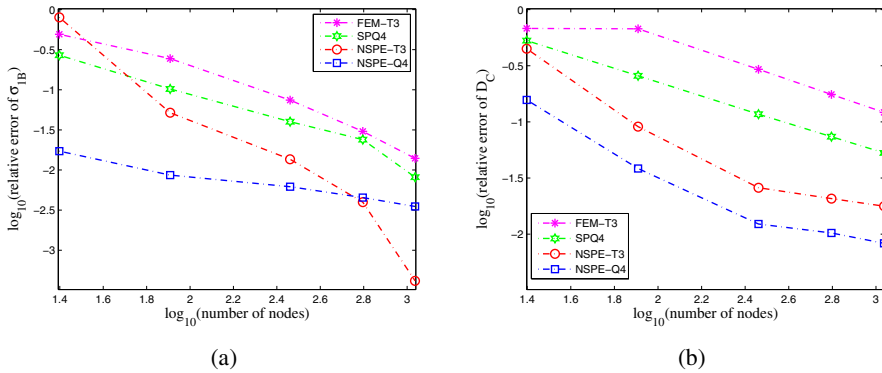


Figure 19: Piezoelectric Cook’s membrane: Convergence behaviours: (a) first principle stress σ_{1B} at point B; (b) electric flux density D_C at point C.

applied, the bimorphs deflect in opposite directions. This bending moves the edges of the mirror up and down, rotating the mirror with an tilt angle β . The angle of rotation β is larger than the angle at the tip of each bending bimorphs, owing to the mechanical amplification that is achieved in this MEMS device. The direction of the reflected light, therefore, can be changed under different applied voltages.

The two-layer bimorphs are made of PVDF material whose properties are summarized as follows.

$$c_{11} = 2.18 \times 10^{-3} \frac{N}{\mu m^2}, \quad c_{13} = 6.33 \times 10^{-4} \frac{N}{\mu m^2},$$

$$c_{33} = 2.18 \times 10^{-3} \frac{N}{\mu m^2}, \quad c_{55} = 7.75 \times 10^{-4} \frac{N}{\mu m^2},$$

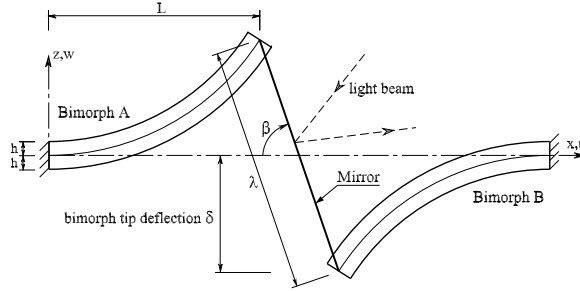


Figure 20: A bimorph optical micro-scanner MEMS device.

$$e_{31} = 4.6 \times 10^{-8} \frac{N}{V\mu m}, \quad e_{33} = 4.6 \times 10^{-8} \frac{N}{V\mu m},$$

$$g_{11} = 1.062 \times 10^{-10} \frac{N}{V^2}, \quad g_{33} = 1.062 \times 10^{-10} \frac{N}{V^2}.$$

The following boundary conditions apply to the bottom layer of the bimorph beam

$$\begin{aligned} \phi^{(1)}(x, -h) &= V_0, \quad \sigma_z^{(1)}(x, -h) = 0, \quad \tau_z^{(1)}(x, -h) = 0, \\ \phi^{(1)}(x, 0) &= 0, \quad \sigma_z^{(1)}(x, 0) = \sigma_z^{(2)}(x, 0), \\ \tau_{xz}^{(1)}(x, 0) &= \tau_{xz}^{(2)}(x, 0), \\ \phi_{,x}^{(1)}(0, z) &= 0, \quad u^{(1)}(0, z) = 0, \quad w^{(1)}(0, z) = 0, \\ \phi_{,x}^{(1)}(L, z) &= 0, \quad \sigma_x^{(1)}(L, z) = 0, \quad \tau_{xz}^{(1)}(L, z) = 0. \end{aligned}$$

and boundary conditions for the top layer are

$$\begin{aligned} \phi^{(2)}(x, 0) &= \phi^{(1)}(x, 0), \quad u^{(2)}(x, 0) = u^{(1)}(x, 0), \\ w^{(2)}(x, 0) &= w^{(1)}(x, 0) \quad \phi^{(2)}(x, h) = V_0, \\ \sigma_z^{(2)}(x, h) &= 0, \quad \tau_{xz}^{(2)}(x, h) = 0, \\ \phi_{,x}^{(2)}(0, z) &= 0, \quad u^{(2)}(0, z) = 0, \quad w^{(2)}(0, z) = 0, \\ \phi_{,x}^{(2)}(L, z) &= 0, \quad \sigma_x^{(2)}(L, z) = 0, \quad \tau_{xz}^{(2)}(L, z) = 0. \end{aligned}$$

Referring to Figure 20, each bimorphs have a length $L = 10\mu m$ and a height $2h = 1\mu m$. The length of the mirror is $\lambda = 1\mu m$. For sufficiently small rotations, β can be approximated as

$$\beta = \frac{2\delta}{\lambda}. \quad (39)$$

A 80×2 uniform mesh with node-based elements (NSPE-T3, NSPE-Q4), the cell-based element (SPQ4) and the FEM-T3 is used to analyse the problem. The tip displacements of the bimorph are calculated for several applied voltage and shown in the Table 5. All the results are compared with the meshless PCM solution [Ohs and Aluru (2001)].

Table 5: Tip deflection of the bimorph beam of the micro-scanner MEMS device.

Applied voltage	FEM-T3	SPQ4	NSPE-Q4	NSPE-T3	Meshless PCM
1.00	4.3765E-03	5.1194E-03	4.7828E-03	4.9138E-03	4.9360E-03
2.00	8.7529E-03	1.0239E-02	9.5656E-03	9.8276E-03	9.8720E-03
5.00	2.1882E-02	2.5597E-02	2.3914E-02	2.4569E-02	2.4681E-02
10.00	4.3765E-02	5.1194E-02	4.7828E-02	4.9138E-02	4.9362E-02
15.00	6.5647E-02	7.6791E-02	7.1742E-02	7.3707E-02	7.4043E-02
20.00	8.7529E-02	1.0239E-01	9.5656E-02	9.8276E-02	9.8724E-02
25.00	1.0941E-01	1.2798E-01	1.1957E-01	1.2285E-01	1.2341E-01
50.00	2.1882E-01	2.5597E-01	2.3914E-01	2.4569E-01	2.4681E-01

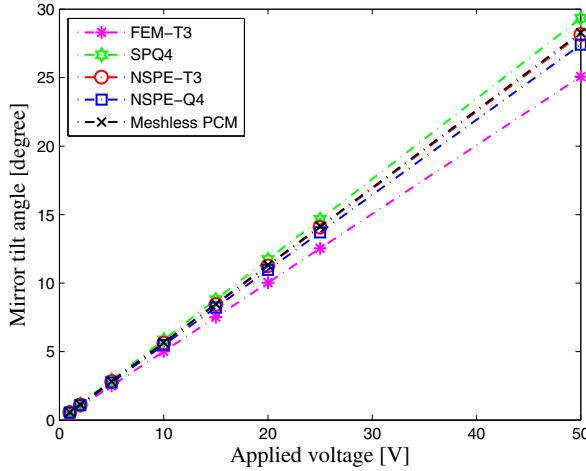


Figure 21: Behaviour of the mirror tilt angle under applied voltages.

From the tip displacements, the tilt angles of the mirror are determined from Equation (39). The tilt angles that vary linearly with applied voltages as expected are shown on Figure 21. It can be seen that the results obtained from node-based and cell-based elements are in closer agreement with the meshless PCM solution than

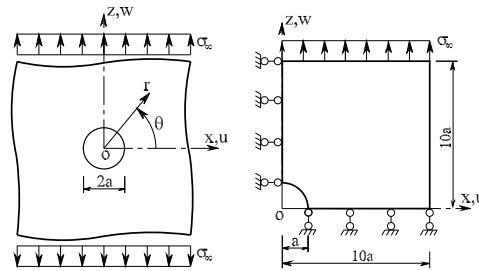


Figure 22: An infinite piezo-plate with a circular hole subjected to the far field stress.

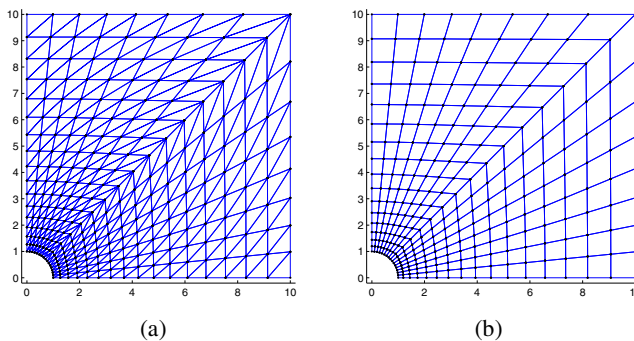


Figure 23: Typical meshes of a quadrant of a piezo-plate with a central circular hole: (a) triangular mesh (NSPE-T3 elements); (b) quadrilateral mesh (NSPE-Q4 elements).

FEM-T3 solutions. It is interesting to note that the result of NSPE-T3 element compares very favorably with the meshless PCM solution but the computational cost is lower.

4.7 An infinite piezoelectric plate with a circular hole

The last problem considered in this section is that of a piezoelectric plate with a central circular cavity subjected to a uniform uniaxial far-field stress σ_∞ in the z -direction as shown in Figure 22. This example is used to show the efficiency of the proposed node-based elements in predicting stresses in a stress concentration problem.

The material is PZT-4 ceramic and its mechanical and piezoelectric elastic constants are as follows.

$$\begin{aligned}
 c_{11} &= 12.6 \times 10^{10}, & c_{33} &= 11.5 \times 10^{10}, & c_{12} &= 7.78 \times 10^{10}, \\
 c_{13} &= 7.43 \times 10^{10}, & c_{55} &= 2.56 \times 10^{10} (N/m^2), \\
 e_{15} &= 12.7, & e_{31} &= -5.2, & e_{33} &= 15.1 (C/m^2), \\
 g_{11} &= 6.463 \times 10^{-9}, & g_{33} &= 5.611 \times 10^{-9} (F/m).
 \end{aligned}$$

Owing to symmetric conditions of the geometry and the loading case, only one quadrant of the problem needs to be modeled. According to Saint-Venant’s principle, stress disturbance due to the hole extends no more than a few diameters from the hole. Thus, it is reasonable to use a $10a$ by $10a$ domain to model one quadrant of the problem domain. In the analysis, the hole radius a is taken to be 1 and the applied stress $\sigma_\infty = 10$. Two types of mesh used in the calculation are shown in Figure 23.

All numerical results are compared well with the analytical solutions given by Sosa (1991) as shown in Figures 24 –27.

Figure 24 and Figure 25 describe the distributions of σ_r and σ_θ on the line $\theta = 0$, respectively. It can be seen from Figure 25 that σ_θ has maximum value at the intersection of the hole and the x -axis as in Sosa’s theoretical results. Obviously, σ_θ and σ_r correspond to the uniaxial stress state at infinity.

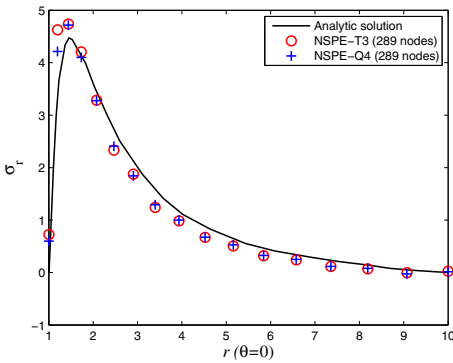


Figure 24: Distribution of σ_r along the line $\theta = 0$.

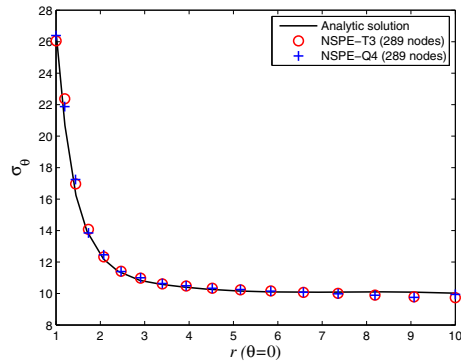


Figure 25: Distribution of σ_θ along the line $\theta = 0$.

The distributions of σ_r and σ_θ on the line $\theta = \pi/2$ are displayed in Figure 26 and Figure 27. It is observed from Figure 27 that σ_θ approaches to zero rapidly when r increases, which indicates there is a stress concentration region near the hole. The minimum value of σ_θ , obtained where the circle intersects the z -axis, agrees well with the theory of piezoelectricity as depicted in Figure 27.

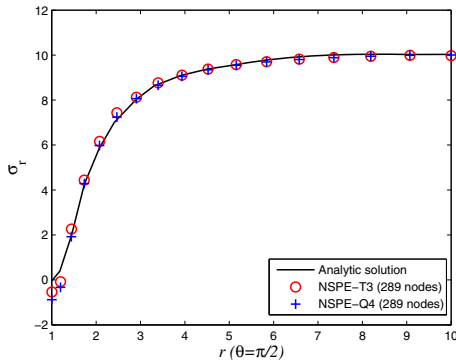


Figure 26: Distribution of σ_r along the line $\theta = \pi/2$.

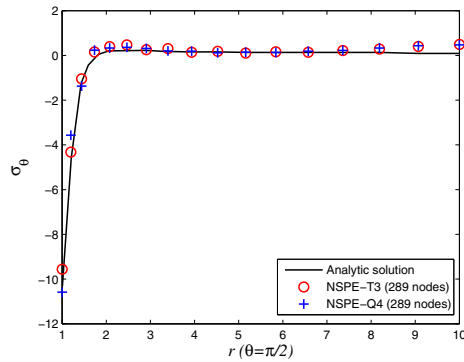


Figure 27: Distribution of σ_t along the line $\theta = \pi/2$.

5 Conclusion

This paper presents a novel node-based smoothing element built on a general triangular or quadrilateral finite element mesh for linear static analysis of planar problems involving piezoelectric materials. The incorporation of the SCNI technique into the node-based finite element has several advantages: (1) field gradients are to be computed directly from shape functions themselves (i.e. derivatives of shape functions are not required) and no limitation is imposed on the shape of elements in the original mesh; (2) the transformation of domain integrations into boundary integrations contributes to the preservation of high accuracy of the method; (3) the method is straightforward and simple to implement because the constructions of the stiffness matrices of the node-based elements are very similar to those of the standard FEM.

The reliability, computational efficiency and convergence of the node-based elements (NSPE-T3 and NSPE-Q4) formulation are demonstrated through various favourable comparisons with other existing elements as well as analytic solutions. It is found that the node-based elements can provide more accurate prediction of the solution than those of the cell-based smoothed SPQ4 elements and the standard FEM-T3 elements with the same degrees of freedom and its performance with respect to analytic solution is excellent even with extreme element distortions. The numerical results presented herein, also indicate that the NSPE-T3 element (based on triangular FE meshes), in general, are better in term of accuracy than the NPSE-Q4 element (based on quadrilateral FE meshes).

Acknowledgement: The supports from the Faculty of Engineering and Survey-

ing (FoES) and the Computational Engineering & Science Research Center (CESRC), USQ, Australia, are gratefully acknowledged. The authors would like to thank the referees and the Editor for their helpful comments.

References

Allik, H.; Hughes, T. J. R. (1970): Finite element method for piezoelectric vibration. *Int. J. Numer. Methods Eng.*, vol. 2, pp. 151–157.

Benjeddou, A. (2000): Advances in piezoelectric finite element modeling of adaptive structural elements: a survey. *Comput. Struct.*, vol. 76, pp. 347–363.

Bisegna, P.; Maceri, F. (1996): An exact three-dimensional solution for simply supported rectangular piezoelectric plate. *Am. Soc. Mech. Eng. Appl. Mech.*, vol. 63, pp. 628–638.

Cambridge, M. (1995): *Product Catalogue: Piezo Systems Inc.*, cambridge ma edition, 1995.

Cannarozzi, A. A.; Ubertini, F. (2001): Some hybrid variational methods for linear electroelasticity problems. *Int. J. Solids Struct.*, vol. 38, pp. 2573–2596.

Carrera, E.; Boscolo, M. (2007): Classical and mixed finite elements for static and dynamic analysis of piezoelectric plates. *Int. J. Numer. Methods Eng.*, vol. 70, pp. 1135–1181.

Chen, J.; Wu, C.; You, Y. (2001): A stabilized conforming nodal integration for Galerkin meshfree method. *International Journal for Numerical Methods in Engineering*, vol. 50, pp. 435–466.

Crawley, E. F.; Luis, J. D. (1987): Use of piezoelectric actuators as elements of intelligent structures. *AIAA Journall*, vol. 25, pp. 1373–1385.

Dai, K. Y.; Liu, G. R. (2007): Free and forced vibration analysis using the smoothed finite element method (SFEM). *J. Sound Vib.*, vol. 301, pp. 803–820.

Dai, K. Y.; Liu, G. R.; Nguyen, T. T. (2007): An n-side polygonal smoothed finite element method (nSFEM) for solid mechanics. *Finite Elem. Anal. Des.*, vol. 43, pp. 847–860.

Dohrmann, C. R.; Heinstein, M. W.; Jung, J.; Key, S. W.; Witkowski, W. R. (2000): Node-based uniform strain elements for three-node triangular and four-node tetrahedral meshes. *Int. J. Numer. Methods Eng.*, vol. 47, pp. 1549–1568.

Gaudenzi, P.; Bathe, K. J. (1995): An iterative finite element procedure for the analysis of piezoelectric continua. *J. Intell. Mater. Syst. Struct.*, vol. 6, pp. 266–273.

Im, S.; Atluri, S. N. (1989): Effect of a piezo-actuator on a finitely deformed beam subjected to general loading. *AIAA Journal*, vol. 27, pp. 1801–1807.

Lam, K. Y.; Ng, T. Y. (1999): Active control of composite plates with integrated piezoelectric sensors and actuators under various dynamic loading conditions. *Smart Mater. Struct.*, vol. 8, pp. 223–237.

Liew, K. M.; Lim, H. K.; Tan, M. J.; He, X. Q. (2002): Analysis of laminated composite beams and plates with piezoelectric patches using the element-free Galerkin method. *Comput. Mech.*, vol. 29, pp. 486–497.

Liu, G. R.; Dai, K. Y.; Lim, K. M.; Gu, Y. T. (2002): A point interpolation mesh free method for static and frequency analysis of two-dimensional piezoelectric structures. *Comput. Mech.*, vol. 29, pp. 510–519.

Liu, G. R.; Dai, K. Y.; Lim, K. M.; Gu, Y. T. (2003): A radial point interpolation method for simulation of two-dimensional piezoelectric structures. *Smart Mater. Struct.*, vol. 12, pp. 171–180.

Liu, G. R.; Dai, K. Y.; Nguyen, T. T. (2007): A smoothed finite element method for mechanics problems. *Comput. Mech.*, vol. 39, no. 6, pp. 859–877.

Liu, G. R.; Nguyen, T. T.; Dai, K. Y.; Lam, K. Y. (2007): Theoretical aspects of the smoothed finite element method (SFEM). *Int. J. Numer. Methods Eng.*, vol. 71, pp. 902–930.

Liu, G. R.; Zhang, G. Y.; Wang, Y. Y.; Zhong, Z. H.; Li, G. Y.; Han, X. (2007): A nodal integration technique for meshfree radial point interpolation method (NI-RPIM). *Int. J. Solids Struct.*, vol. 44, pp. 3840–3860.

Long, C. S.; Loveday, P. W.; Groenwold, A. A. (2006): Planar four node piezoelectric elements with drilling degrees of freedom. *Int. J. Numer. Methods Eng.*, vol. 65, pp. 1820–1830.

Mackerle, J. (2003): Smart materials and structures - an finite element approach - an addendum: a bibliography (1997-2002). *Modelling and Simulation in Materials Science and Engineering*, vol. 11, pp. 707–744.

Nguyen-Van, H.; Mai-Duy, N.; Tran-Cong, T. (2007): A simple and accurate four-node quadrilateral element using stabilized nodal integration for laminated plates. *CMC: Computers, Materials & Continua*, vol. 6, no. 3, pp. 159–176.

Nguyen-Van, H.; Mai-Duy, N.; Tran-Cong, T. (2008): A smoothed four-node piezoelectric element for analysis of two-dimensional smart structures. *CMES: Computer Modeling in Engineering & Sciences*, vol. 23, no. 3, pp. 209–222.

Nguyen-Van, H.; Mai-Duy, N.; Tran-Cong, T. (2008): Free vibration of laminated plate/shell structures based on FSDT with a stabilized nodal-integrated quadrilateral element. *J. Sound Vib.*, vol. 313, no. 1-2, pp. 205–223.

Ohs, R. R.; Aluru, N. R. (2001): Meshless analysis of piezoelectric devices. *Comput. Mech.*, vol. 27, pp. 23–36.

Ray, M. C.; Bhattacharya, R.; Samanta, B. (1998): Exact solutions for dynamic analysis of composite plates with distributed piezoelectric layers. *Comput. Struct.*, vol. 66, no. 6, pp. 737–743.

Shen, I. Y. (1995): Bending and torsional vibration control of composite beam through intelligent constrained-layer damping treatments. *Smart Mater. Struct.*, vol. 4, no. 1, pp. 340–355.

Sladek, J.; Sladek, V.; Zhang, C.; Garcia-Sanche, F.; Wunsche, M. (2006): Meshless Local Petrov-Galerkin Method for Plane Piezoelectricity. *CMC: Computers, Materials & Continua*, vol. 4, no. 2, pp. 109–117.

Sladek, J.; Sladek, V.; Zhang, C.; Solek, P.; Starek, L. (2007): Fracture Analyses in Continuously Nonhomogeneous Piezoelectric Solids by the MLPG. *CMES: Computer Modeling in Engineering & Sciences*, vol. 19, no. 3, pp. 247–262.

Sosa, H. (1991): Plane problems in piezoelectric media with defects. *Int. J. Solids Struct.*, vol. 28, pp. 491–505.

Sze, K. Y.; Pan, Y. S. (1999): Hybrid finite element models for piezoelectric materials. *J. Sound Vib.*, vol. 226, pp. 519–547.

Sze, K. Y.; Yang, X.-M.; Yao, L.-Q. (2004): Stabilized plane and axisymmetric piezoelectric finite element models. *Finite Elem. Anal. Des.*, vol. 40, pp. 1105–1122.

Sze, K. Y.; Yao, L. Q. (2000): Modelling smart structures with segmented piezoelectric sensors and actuators. *J. Sound Vib.*, vol. 235, pp. 495–520.

Tzou, H. S.; Tiersten, H. F. (1994): Elastic analysis of laminated composite plates in cylindrical bending due to piezoelectric actuators. *Smart Mater. Struct.*, vol. 3, pp. 255–265.

Wu, C. C.; Sze, K. Y.; Huang, Y. Q. (2001): Numerical solutions on fracture of piezoelectric materials by hybrid element. *Int. J. Solids Struct.*, vol. 38, pp. 4315–4329.